

A local study of dynamo action driven by precession

Vivaswat Kumar,^{1,2,*} Federico Pizzi,^{1,3} George Mamatsashvili,^{1,4}
André Giesecke,¹ Frank Stefani,¹ and Adrian J. Barker⁵

¹*Institute of Fluid Dynamics, Helmholtz-Zentrum Dresden-Rossendorf,
Bautzner Landstraße 400, 01328 Dresden, Germany*

²*Institute of Process Engineering and Environmental Technology,
Technische Universität Dresden, 01062 Dresden, Germany*

³*Department of Fluid Mechanics, Universitat Politècnica de Catalunya-BarcelonaTech,
Barcelona 08034, Spain*

⁴*E. Kharadze Georgian National Astrophysical Observatory, Abastumani 0301, Georgia*

⁵*Department of Applied Mathematics, School of Mathematics,
University of Leeds, Leeds, LS2 9JT, United Kingdom*

(Dated: December 13, 2023)

We demonstrate an efficient magnetic dynamo due to precession-driven hydrodynamic turbulence in the local model. Dynamo growth rate increases with Poincaré and magnetic Prandtl numbers. Spectral analysis shows that the dynamo acts over a broad range of scales: at large (system size) and intermediate scales it is driven by 2D vortices and shear of the background precessional flow, while at smaller scales it is mainly driven by 3D inertial waves. These results are important for understanding magnetic field generation and amplification in precessing planets and stars.

Understanding the generation, amplification and self-sustenance of magnetic fields in astrophysical and geophysical objects is the endeavour of dynamo theory [1, 2]. From the magnetic field of our planet to distant stars and galaxies, magnetohydrodynamic (MHD) dynamo models offer insights into complex interplay between flows of conducting fluids and fields, leading to the growth of the latter. To achieve this, dynamo must be sufficiently efficient in transforming kinetic energy of a flow into magnetic energy, which in turn requires a strong driving mechanism of the flow.

Among the known driving mechanisms for planetary dynamos, precession-powered motion is a complementary candidate [3, 4] to a more generally accepted convection [5]. Precession takes place when the rotation axis of a system changes its orientation, producing a volume force that drives a flow in the (liquid) interior of the precessing body [6]. Precession-driven flows are potentially able to convert large amounts of kinetic energy (up to $10^{11} - 10^{21}$ W [4, 7, 8]) to sustain the geomagnetic field [3]. This conversion is due to instabilities [6, 9] that give rise to vortex tangles and may also induce turbulence within superfluid neutron stars [10, 11].

Precession-driven flows have been studied both numerically [12–19] and experimentally [20–23] and their ability to drive dynamo was demonstrated for laboratory flows in a specific parameter regime [13, 23]. In astrophysics and geophysics, precessing flows are studied using a widely employed local model [24–27], which describes a small segment of a celestial body (stars, gaseous planets or the liquid cores of rocky planets) in a Cartesian coordinate frame (x, y, z) rotating around the z -axis and precessing around another tilted axis with angular velocities Ω and $\text{Po} \cdot \Omega$, respectively, where Po is Poincaré number characterizing precession strength. In this local frame, the

precession-driven flow has a linear shear along the vertical z -axis, which oscillates in time and is proportional to Po , $\mathbf{U}_0 = -2\Omega \cdot \text{Po} \cdot z(\sin(\Omega t), \cos(\Omega t), 0)^T$ [24, 25, 27]. This background flow is subject to a precessional instability and breaks down into a nonlinear (turbulent) state consisting of 2D vortices and 3D inertial waves [25–27].

In this Letter, following our hydrodynamical study [27], we consider the MHD case and demonstrate a magnetic dynamo action powered by the precession-driven *turbulence* resulting from the nonlinear saturation of the precessional instability. Previous studies [12, 13, 16, 18, 19, 28] on the precession dynamo in global settings, mostly in the context of laboratory experiments, emphasized the significance of large-scale vortices as a primary driver for large-scale magnetic field amplification, suggesting that the nature of the dynamo is closely linked to this flow pattern. This work, going beyond those findings, demonstrates for the first time the strong influence of the precession on the dynamo properties over a much broader range of scales not captured in the current global models. Focusing on the kinematic stage, we show a remarkable transition from a vortex-driven large-scale dynamo at small Po to a more complex type driven both by vortices and waves at different scales at higher Po . These two regimes of the dynamo are governed by the intrinsic dynamics of precession-driven flows, namely their transition from the dominant geostrophic vortices to 3D inertial wave turbulence with increasing Po [27].

Consider a velocity perturbation \mathbf{u} about the background flow \mathbf{U}_0 in the rotating and precessing frame. The main MHD equations for a conducting incompressible fluid in this local frame are [25, 27]

$$(\partial_t + \mathbf{U}_0 \cdot \nabla + \mathbf{u} \cdot \nabla) \mathbf{u} = -\frac{1}{\rho} \nabla \Pi + \frac{1}{\rho} (\mathbf{B} \cdot \nabla) \mathbf{B} + \nu \nabla^2 \mathbf{u} - 2\Omega \mathbf{e}_z \times \mathbf{u} - 2\Omega \boldsymbol{\varepsilon}(t) \times \mathbf{u} + 2\Omega u_z \mathbf{e}_z \times \boldsymbol{\varepsilon}(t), \quad (1)$$

$$(\partial_t + \mathbf{U}_0 \cdot \nabla) \mathbf{B} = \nabla \times (\mathbf{u} \times \mathbf{B}) + \eta \nabla^2 \mathbf{B} - 2\Omega B_z \mathbf{e}_z \times \boldsymbol{\varepsilon}(t), \quad (2)$$

supplemented with $\nabla \cdot \mathbf{u} = \nabla \cdot \mathbf{B} = 0$, where ρ is the constant density of the fluid, Π is the sum of thermal and magnetic pressures, \mathbf{B} is the magnetic field, ν is the kinematic viscosity, η is the magnetic diffusivity and the vector $\boldsymbol{\varepsilon}(t) = \text{Po}(\cos(\Omega t), -\sin(\Omega t), 0)^T$ describes the effects of precession in these equations. Specifically, Coriolis acceleration due to precession, $-2\Omega \boldsymbol{\varepsilon}(t) \times \mathbf{u}$, and the stretching term $2\Omega u_z \mathbf{e}_z \times \boldsymbol{\varepsilon}(t)$ of the perturbation velocity due to the shear of the base flow in Eq. (1) jointly give rise to the precessional instability [29, 30]. A similar stretching term $-2\Omega B_z \mathbf{e}_z \times \boldsymbol{\varepsilon}(t)$ in Eq. (2) describes the growth of the magnetic field due to the shear.

The flow is considered in a periodic cubic box with the length L in each direction, $L_x = L_y = L_z = L$. We normalize time by Ω^{-1} , length by L , velocity by ΩL and pressure as well as kinetic $E_v = \rho \mathbf{u}^2/2$ and magnetic $E_m = \mathbf{B}^2/2$ energy densities by $\rho L^2 \Omega^2$. The main parameters are the Poincaré, Po , the Reynolds, $\text{Re} = \Omega L^2/\nu$, and magnetic Prandtl, $\text{Pm} = \nu/\eta$, numbers. Below we fix $\text{Re} = 3 \times 10^4$ and explore a broad range of $\text{Po} = 0.075 - 0.4$ and $\text{Pm} = 10^{-1} - 10$.

We solve Eqs. (1) and (2) using the spectral code SNOOPY [31] adapted to the local precessional flow [25]. Resolution for $\text{Pm} < 1$, i.e., when the viscous scales are shortest, is set as in [27]: $(N_x, N_y, N_z) = (128, 128, 128)$ at $\text{Po} \leq 0.125$ and $(256, 256, 256)$ at $\text{Po} > 0.125$, while for $\text{Pm} > 1$, when resistive scales are shortest instead, it is increased by a factor $\text{Pm}^{1/2}$. Random velocity perturbations with rms $\langle \mathbf{u}^2 \rangle^{1/2} = 1.12 \times 10^{-4}$ and a very weak random magnetic field with rms $\langle \mathbf{B}^2 \rangle^{1/2} = 10^{-12}$, are imposed initially, so that the back-reaction of the magnetic field on the flow is negligible.

Figure 1 shows the evolution of the volume-averaged kinetic $\langle E_v \rangle$ and magnetic $\langle E_m \rangle$ energies at different Po and Pm , which indicates a two-staged dynamo process. In the beginning, the kinetic energy grows exponentially as a result of the linear precessional instability, while the magnetic energy decreases. After several precession times $\sim (\epsilon\Omega)^{-1}$, the exponential growth saturates due to non-linearity [advection $(\mathbf{u} \cdot \nabla) \mathbf{u}$ in Eq. (1)] and the flow settles down into a quasi-steady turbulence composed of 2D vortices and 3D inertial waves [25, 27]. Remarkably, the dynamo action – exponential growth of the magnetic field – starts only *after* saturation of the precession instability and is driven by the nonlinear (turbulent) velocity perturbations. After several hundred orbits, the magnetic field growth saturates nonlinearly due to the back-reaction of Lorentz force on the flow, which is discernible by the small drop in $\langle E_v \rangle$ at the saturation point

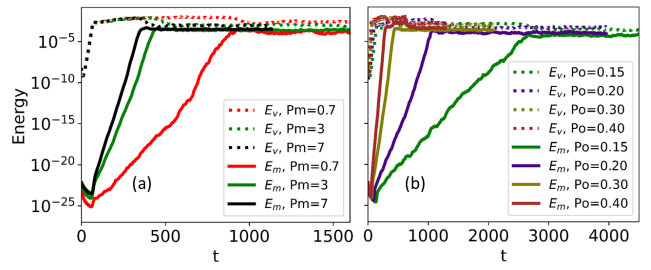


FIG. 1. Evolution of the volume-averaged kinetic $\langle E_v \rangle$ (dotted) and magnetic $\langle E_m \rangle$ (solid) energies at $\text{Re} = 3 \times 10^4$ for (a) different Pm at $\text{Po} = 0.3$ and (b) different Po at $\text{Pm} = 3$.

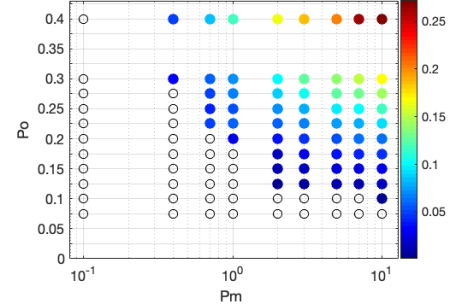


FIG. 2. Dynamo growth rate γ in the (Pm, Po) -plane indicated by color points, whereas there is no dynamo at empty points. Both color and empty points represent all the simulations done.

of $\langle E_m \rangle$ (Fig. 1). The growth rate of the magnetic energy, $\gamma = d \ln \langle E_m \rangle / dt$, in the kinematic regime and its nonlinear saturation level increase, and hence the dynamo is more efficient, with increasing Po and/or Pm . This dependence on Po and Pm is further explored in Fig. 2, which shows γ in the (Po, Pm) -plane and summarizes all our runs. Note that the critical Po_c for the dynamo onset decreases with increasing Pm .

Figure 3 shows the structures of the vertical vorticity $\omega_z = (\nabla \times \mathbf{u})_z$ in physical space at $\text{Po} = 0.15$ and, at the same instants, the induced vertical field B_z during the kinematic stage in two runs at $\text{Pm} = 3$ and 7. We observe vertically nearly uniform larger-scale columnar vortices embedded in a sea of smaller-scale 3D inertial waves, as typical of precession-driven turbulence [25–27]. The traces of these vortices are visible in the magnetic field, since vortices are in fact the main drivers of the dynamo at this small Po (see Fig. 5). Note the decrease in characteristic length of B_z structures as Pm increases.

To analyse dynamo action across length-scales, we decompose the magnetic field into Fourier modes [25, 27]

$$\mathbf{B}(\mathbf{r}, t) = \sum_{\mathbf{k}} \bar{\mathbf{B}}(\mathbf{k}(t), t) e^{i\mathbf{k}(t) \cdot \mathbf{r}}, \quad (3)$$

where $\mathbf{k}(t) = (k_x, k_y, k_z(t))^T$ is the wavevector with $k_z(t) = k_{z0} + 2\text{Po}(-k_x \cos(t) + k_y \sin(t))$ oscillating in time about a constant k_{z0} due to the periodic time-variation

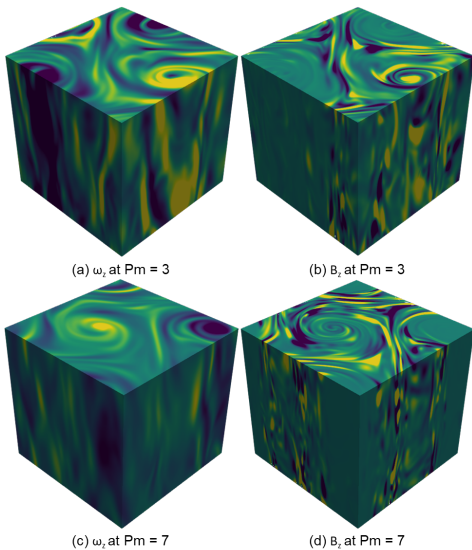


FIG. 3. Spatial structures of the vertical vorticity $\omega_z = (\nabla \times \mathbf{u})_z$ at $Po = 0.15$ in two runs at (a) $Pm = 3$ and (c) $Pm = 7$ alongside the corresponding induced vertical field B_z in (b) and (d), respectively. For each Pm , the snapshots of ω_z and B_z are shown at equal instants during the kinematic regime.

of the background flow \mathbf{U}_0 .

Figure 4 shows the shell-averaged [32] magnetic energy spectrum, $\mathcal{E}_m = |\bar{\mathbf{B}}|^2/2$, in the middle of and at the end of the kinematic stage together with the corresponding growth rate $\gamma(k)$ versus wavenumber $k = |\mathbf{k}|$ at different Po and Pm . Note that in all the cases, the growth rate is nearly constant and positive, $\gamma(k) > 0$, at lower and intermediate $k \lesssim 200$, indicating the dynamo action at these wavenumbers, and decreases, turning negative, at higher k due to resistivity. At small $Po = 0.15$, the growth rate weakly increases with Pm , mostly at higher wavenumbers [Fig. 4(a)]. As a result, the energy spectra at $Pm = 3$ and 7 have nearly the same shape and magnitude at small and intermediate wavenumbers, both during and at the end of the growth, while high wavenumbers have more power for $Pm = 7$ than that for $Pm = 3$. The magnetic energy spectrum and $\gamma(k)$ depend more strongly on Pm at higher $Po = 0.3$ and 0.4 , as seen in Figs. 4(b) and 4(c), respectively. For a given Po , the positive growth rate (nearly independent of k at lower k) increases with Pm and extends to higher k 's the larger Pm is, so the spectrum grows faster at high k with increasing Pm and hence is less steep.

Comparing now the spectral behavior for different Po and given Pm in Fig. 4, we notice that with increasing Po , $\gamma(k)$ moderately increases, although the maximum k where there is still a dynamo does not appear to change much from $Pm = 0.7$ to 3 . This threshold wavenumber increases with Po at higher $Pm = 7$, being associated with driving by small-scale waves at high k (see below). As a result, the magnetic energy spectra are shallower at high k for $Po = 0.4$ and 0.3 than those for $Po = 0.15$.

The precession-driven hydrodynamic turbulence, as

noted above, consists of 2D vortices and 3D inertial waves [25–27] similar to classical (forced) rotating turbulence [33, 34]. The *slow* 2D vortical mode varies only in the horizontal (x, y) -plane and is uniform along the z -axis, having $k_z = 0$. The velocity of this mode, denoted as \mathbf{u}_{2D} , has the dominant horizontal component $u_h = (u_x^2 + u_y^2)^{1/2} \gg u_z$. On the other hand, the *fast* 3D inertial wave mode with nonzero frequency $\pm 2\Omega k_z/k$, varies along the z -axis, $k_z \neq 0$, and its velocity \mathbf{u}_{3D} has comparable horizontal and vertical components, $u_h \sim u_z$. We will show that these modes play a crucial role in the dynamo action and its dependence on Po .

To understand the roles of the background flow \mathbf{U}_0 as well as the vortices and inertial waves in driving the precession dynamo, we first obtain the equation for the magnetic energy spectrum \mathcal{E}_M by substituting transformation (3) into Eq. (2) and multiplying by conjugate $\bar{\mathbf{B}}^*$. Then, in the electromotive force (EMF) $\nabla \times (\mathbf{u} \times \mathbf{B})$, the velocity is divided into vortical \mathbf{u}_{2D} and wave \mathbf{u}_{3D} components, $\mathbf{u} = \mathbf{u}_{2D} + \mathbf{u}_{3D}$, giving

$$\frac{d\mathcal{E}_M}{dt} = P + D_M + I_{2D} + I_{3D}, \quad (4)$$

where $P = \Omega(\bar{\mathbf{B}}^* \bar{B}_z + \bar{\mathbf{B}} \bar{B}_z^*)(\boldsymbol{\varepsilon}(t) \times \mathbf{e}_z)$ describes energy exchange between magnetic field and the background flow due to shear; when $P > 0$ energy is injected from the flow into the field. The second term $D_M = -2k^2 \mathcal{E}_M / (Re \cdot Pm) < 0$ is resistive dissipation. The third I_{2D} and fourth I_{3D} terms related to \mathbf{u}_{2D} and \mathbf{u}_{3D} in the Fourier transform of EMF (denoted with bar) are given by $I_{2D} = i[\bar{\mathbf{B}}^* \mathbf{k} \times (\overline{\mathbf{u}_{2D} \times \mathbf{B}}) - \bar{\mathbf{B}} \mathbf{k} \times \overline{(\mathbf{u}_{2D} \times \mathbf{B})}^*] / 2$ and $I_{3D} = i[\bar{\mathbf{B}}^* \mathbf{k} \times (\overline{\mathbf{u}_{3D} \times \mathbf{B}}) - \bar{\mathbf{B}} \mathbf{k} \times \overline{(\mathbf{u}_{3D} \times \mathbf{B})}^*] / 2$ and describe magnetic energy production, respectively, by vortices and inertial waves.

Figure 5 shows the shell-averaged spectra of these four terms in the middle of the kinematic stage. Depending on Po and Pm , either only vortices, or cooperatively vortices and waves are mainly responsible for the magnetic field amplification. At the lowest $Po = 0.15$, both for $Pm = 3$ and 7 , the dynamo is mainly driven by vortices, because I_{2D} is positive and much larger than I_{3D} and P [Figs. 5(a) and 5(b)]. As Pm increases, I_{2D} extends a bit to higher k , although its dependence on Pm seems to be weak at this Po , consistent with the behavior in Fig. 4(a). At higher $Po = 0.3$ the role of inertial waves in driving the dynamo becomes more appreciable: I_{3D} is now comparable to I_{2D} and P , but mostly operates at higher $k \gtrsim 100$ than the latter two terms (since the relevant waves are of small-scale), as seen in Figs. 5(c) and 5(d) for the same Pm . With increasing Pm , I_{3D} dominates over I_{2D} and P at large k , so the 3D waves become the main drivers of the dynamo at small scales, while the vortices and injection from the base flow dominate at lower k , i.e., larger scales [Fig. 5(d)].

To conclude, we revealed and analyzed dynamo action powered by precession-driven *turbulence*, which is capa-

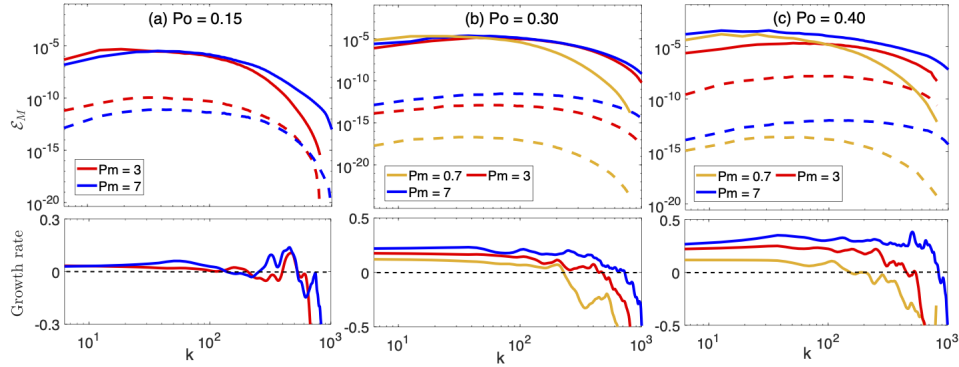


FIG. 4. (Top row) Shell-averaged magnetic energy spectra in the middle (dashed) and at the end (solid) of the kinematic stage of the dynamo at various Pm for (a) $Po = 0.15$, (b) 0.3 and (c) 0.4 . (Bottom row) The corresponding growth rate $\gamma(k)$ of the spectral magnetic energy. There is no dynamo at $Po = 0.15$ and $Pm = 0.7$, hence the yellow curve is absent in panel (a).

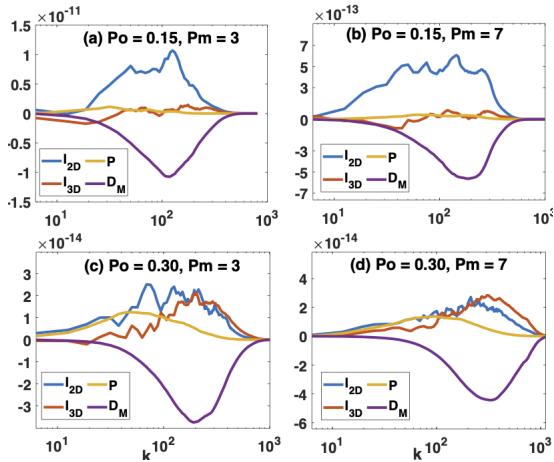


FIG. 5. Shell-averaged spectra of the dynamical terms in Eq. (4): energy injection from the flow, P , resistive dissipation, D_M , and the contributions from 2D vortices, I_{2D} , and 3D inertial waves, I_{3D} , in the middle of the kinematic stage at (a) $Po = 0.15$, $Pm = 3$; (b) $Po = 0.15$, $Pm = 7$; (c) $Po = 0.3$, $Pm = 3$ and (d) $Po = 0.3$, $Pm = 7$.

ble of exponentially amplifying magnetic field. Although our model is local, it captures two basic ingredients of the turbulence: large-scale 2D vortices and smaller-scale 3D inertial waves. This model covers thus a broader range of length-scales – from the system size to the shortest dissipation scales – than existing global models of precessional flows [12–19], thereby providing deeper insights into the precession dynamo properties (growth rate, energy spectra, driving mechanism) over these scales. We showed that during the kinematic stage, the growth rate of the dynamo increases with the Poincaré (Po) and the magnetic Prandtl (Pm) numbers. The critical Pm_c for the dynamo onset also increases with decreasing Po . At small $Po \lesssim 0.15$ the dynamo is mainly driven by 2D vortices at large (system size) and intermediate scales, being therefore less sensitive to Pm . At larger $Po \gtrsim 0.15$, driving by waves at smaller scales becomes important and

hence the dynamo growth rate increases with Pm and Po , while at larger scales the dynamo is still driven by 2D vortices and the shear of the background precessional flow.

Finally, we note the sequence of processes leading to the dynamo action here (a precessional flow subject to instability \rightarrow turbulence \rightarrow vortices \rightarrow dynamo) resembles that taking place in rotating convection. As shown in [35], thermal convection in the presence of rotation leads to turbulence and formation of large-scale vortices, which in turn amplify large-scale magnetic field. Thus, these two different (convection and precession) processes share a common generic mechanism – *vortex-induced dynamo*, which we have analyzed here. Thus, this study can be important not only for understanding the magnetic dynamo action in precessing planets and stars, but also in a more general context of flow systems where vortices emerge and govern the flow dynamics.

This project has received funding from the European Research Council (ERC) under the European Union’s Horizon 2020 research and innovation program (Grant Agreement No. 787544). AJB was funded by STFC grants ST/S000275/1 and ST/W000873/1

* v.kumar@hzdr.de

- [1] P. H. Roberts, *Fundamentals of dynamo theory*, in *Lectures on Solar and Planetary Dynamos*, Publications of the Newton Institute, edited by M. R. E. Proctor and A. D. Gilbert (1994) p. 1–58.
- [2] K. Moffatt and E. Dormy, *Self-Exciting Fluid Dynamos*, Cambridge Texts in Applied Mathematics (Cambridge University Press, 2019).
- [3] W. V. R. Malkus, *Science* **160**, 259 (1968).
- [4] J. Vanyo, *Geophys. Astro. Fluid.* **59**, 209 (1991).
- [5] M. Landeau, A. Fournier, H.-C. Nataf, D. Cébron, and N. Schaeffer, *Nature Reviews Earth & Environment* **3**, 255 (2022).
- [6] R. Lagrange, P. Meunier, F. Nadal, and C. Eloy, *J. Fluid Mech.* **666**, 104 (2011).

- [7] D. E. Loper, *Phys. Earth Planet. Inter.* **11**, 43 (1975).
- [8] M. Rochester, J. Jacobs, D. Smylie, and K. Chong, *Geophys. J. Int.* **43**, 661 (1975).
- [9] A. Giesecke, T. Albrecht, T. Gundrum, J. Hecault, and F. Stefani, *New J. Phys.* **17**, 113044 (2015).
- [10] K. Glampedakis, N. Andersson, and D. Jones, *Phys. Rev. Lett.* **100**, 081101 (2008).
- [11] K. Glampedakis, N. Andersson, and D. Jones, *Mon. Not. R. Astron. Soc.* **394**, 1908 (2009).
- [12] A. Tilgner, *Phys. Fluids* **17**, 034104 (2005).
- [13] A. Giesecke, T. Vogt, T. Gundrum, and F. Stefani, *Phys. Rev. Lett.* **120**, 024502 (2018).
- [14] F. Pizzi, A. Giesecke, and F. Stefani, *AIP Adv.* **11**, 035023 (2021).
- [15] F. Pizzi, A. Giesecke, J. Šimkanin, and F. Stefani, *New J. Phys.* **23**, 123016 (2021).
- [16] D. Cébron, R. Laguerre, J. Noir, and N. Schaeffer, *Geophys. J. Int.* **219**, S34 (2019).
- [17] D. Kong, Z. Cui, X. Liao, and K. Zhang, *Geophys. Astro. Fluid.* **109**, 62 (2015).
- [18] O. Goepfert and A. Tilgner, *New J. Phys.* **18**, 103019 (2016).
- [19] Y. Lin, P. Marti, J. Noir, and A. Jackson, *Phys. Fluids* **28**, 066601 (2016).
- [20] J. Noir, D. Brito, K. Aldridge, and P. Cardin, *Geophys. Res. Lett.* **28**, 3785 (2001).
- [21] P. Meunier, C. Eloy, R. Lafrange, and F. Nadal, *J. Fluid Mech.* **599**, 405–440 (2008).
- [22] S. Goto, A. Matsunaga, M. Fujiwara, M. Nishioka, S. Kida, M. Yamato, and S. Tsuda, *Phys. Fluids* **26**, 055107 (2014).
- [23] V. Kumar, F. Pizzi, A. Giesecke, J. Šimkanin, T. Gundrum, M. Ratajczak, and F. Stefani, *Phys. Fluids* **35**, 014114 (2023).
- [24] R. M. Mason and R. R. Kerswell, *J. Fluid Mech.* **471**, 71–106 (2002).
- [25] A. J. Barker, *Mon. Not. R. Astron. Soc.* **460**, 2339 (2016).
- [26] A. Khelif, A. Salhi, S. Nasraoui, F. Godeferd, and C. Cambon, *Phys. Rev. E* **98**, 011102 (2018).
- [27] F. Pizzi, G. Mamatsashvili, A. Barker, A. Giesecke, and F. Stefani, *Phys. Fluids* **34** (2022).
- [28] F. Pizzi, A. Giesecke, J. Šimkanin, K. Vivaswat, G. Thomas, and F. Stefani, *Magnetohydrodynamics* **58**, 445 (2022).
- [29] R. R. Kerswell, *Geophys. Astro. Fluid.* **72**, 107 (1993).
- [30] A. Salhi, T. Lehner, and C. Cambon, *Phys. Rev. E* **82**, 016315 (2010).
- [31] G. Lesur and P. Y. Longaretti, *Astron. Astrophys.* **444**, 25 (2005).
- [32] As usual in turbulence theory, shell-average of a spectral quantity \bar{f} in Fourier space is defined as, $\sum_{k \leq |\mathbf{k}| \leq k + \Delta k} \bar{f}(\mathbf{k})$, with the sum being over spherical shells with radius $k = (k_x^2 + k_y^2 + k_z^2)^{1/2}$ and width Δk [34], where $k_i = n_i \Delta k$, $i = (x, y, z)$, are the discrete wavenumbers in the cubic box with integer $n_i = 0, \pm 1, \pm 2, \dots, \pm(N_i/2 - 1)$ and $\Delta k = 2\pi/L$ is the grid cell size in Fourier space, i.e., the minimum nonzero wavenumber in this box.
- [33] M. Buziccotti, H. Aluie, L. Biferale, and M. Linkmann, *Phys. Rev. Fluids* **3**, 034802 (2018).
- [34] A. Alexakis and L. Biferale, *Phys. Rep.* **767**, 1 (2018).
- [35] C. Guervilly, D. W. Hughes, and C. A. Jones, *Phys. Rev. E* **91**, 041001 (2015).